ISSN 2712-0554
Heritage and Sustainable Development *Original Research*
Vol. 6, No. 1, January 2024, pp.43-66
https://doi.org/10.37868/hsd.v6i1.346

Numerical simulation of integrating an air conditioner with an evaporative air cooler

Haider Mumtaz Hussain[1*], Salman Hashim Hammdi[2]
[1,2] Collage of Engineering, University of Basrah, Iraq

*Corresponding author E-mail: Haideralbayati200487@yahoo.com

Received Nov. 24, 2023
Revised Dec. 17, 2023
Accepted Jan. 11, 2024

Abstract

During the summer, air conditioning is increasingly used in commercial and residential structures to provide thermal comfort. The elevated condenser pressure caused by high ambient temperatures has led to a significant increase in electricity consumption in dry, hot climates. Therefore, this article presents the results of a numerical simulation investigation into the feasibility of enhancing the performance of a conventional air conditioning unit by applying a direct evaporative cooling system. The objective is to increase the cooling capacity while decreasing power consumption. The program used a small window-type air conditioner configured to simulate various weather conditions. The numerical findings indicate that incorporating evaporative cooling aids improved the system's ability to overcome numerous obstacles, resulting in a 10–20% increase in refrigeration capacity. Additionally, power consumption was reduced by approximately 3%, and the discharge temperature fell by 6–10°C. The predicted mean vote standard (PMV) for thermal conditions for human occupants yielded favorable outcomes (normal-type). Despite the challenging climate conditions prevailing during the five sweltering summer months, water production demonstrated good results, particularly in September.

Keywords: Window-type air conditioner, PMV, Evaporated air cooler, Hot climate, Water productivity, Numerical simulation

1. Introduction

Energy is vital for a country's economy to grow. As energy consumption continues to rise, saving it becomes increasingly important. Many engineering fields are striving to optimize energy utilization or reduce consumption [1–3]. Reducing energy usage can lower dependence on costly oil and gas, significantly impacting a country's economy [4]. Conserving energy plays a crucial role in mitigating global warming.

Using more energy enables a more comfortable lifestyle. Air conditioners, refrigerators, and water heaters consume around 30% of total power requirements [5]. Air conditioners in homes and businesses account for nearly half of all electricity usage [6]. Experts predict a 71% surge in energy demand between 2003 and 2030 due to population growth and expanding economies [7]. Therefore, optimizing energy usage, especially in cooling buildings, is crucial to global energy conservation efforts.

Efficient cooling systems help conserve energy. Strategies include reducing compressor power usage, enhancing heat rejection in the condenser, or minimizing pressure differences between the condenser and evaporator. Elevated condenser temperatures increase compressor workload, potentially reducing efficiency and lifespan. In high temperatures, most air-cooled systems' efficiency drops to around 2.2–2.4 [8]. Extended exposure to extreme heat, like temperatures surpassing 45°C, can cause air conditioners to malfunction due to excessive condenser pressure.

In some Middle Eastern nations, summer temperatures soar beyond 40–45°C. The air conditioner's constant operation in such conditions escalates electricity consumption and reduces system efficiency [9]. Employing evaporative condensers to cool the air before reaching the coil lowers condenser temperature and pressure. Evaporative condensers can mitigate high outdoor temperatures, especially in regions with drastic dry and wet temperature differences during peak periods [10]. Despite lower airflow and heat transfer area [11], these condensers efficiently reduce energy consumption and alleviate pressure on power systems [12], [13]. Ongoing research aims to enhance evaporative-cooled condensers' heat transfer for more efficient cooling systems.

This paper examines the functionality of evaporative condensers, the energy consumption of residential cooling systems, and the fundamental principles, regulations, and theory underlying the heat removal process of evaporative condensers, crucial for facilitating heat transfer from the refrigerant during its transition from a gaseous to a liquid state. Condensers are indispensable components of cooling systems, with vapor, water, and air condensers being among the various types available. Smaller refrigeration systems, like chillers, typically utilize air-cooled condensers up to about 20 tons [14], [15]. Heat transfer in air-cooled condensers occurs between coils and the ambient air, operating based on the principles of thermal transfer governed by air physics. However, their effectiveness might be affected by weather conditions. Air-cooled models are most common, as they do not rely on water, although they tend to be noisier due to their high ventilation requirements. Despite being more cost-effective in production and operation, alternative condensers consume less energy. Air-cooled systems must maintain a condensing temperature of approximately 15–20°C higher than ambient air [16]. An alternative method involves using adjacent water to eliminate heat, which is then converted to heated air by a tower [17], [18].

Although this condenser type is smaller and more efficient in heat transfer compared to air-cooled units, it necessitates water and a larger initial investment [19] [20], requiring a pump for water circulation. Chemical treatment is essential to prevent coil fouling, and regular monitoring and maintenance are necessary. If the distance between the compressor and the heat release point is substantial for pushing the refrigerant vapor, only the water-cooled condenser should be used, typically handling from half to ten thousand tons of refrigeration (TR). Water-cooled condensers are primarily employed in heat pumps and specialized equipment [21].

Next, let's discuss the evaporative condenser. In larger non-residential settings requiring substantial cooling, evaporative cooling effectively removes heat more efficiently than air-cooled systems. These compact heat exchangers facilitate the exchange of air and water for cooling. They transfer sensible and latent heat between the air and water, where the water transforms into vapor, subsequently cooling the air. Unlike air-cooled systems, these condensers require smaller fans and motors, resulting in reduced air demand. Additionally, they necessitate fewer chemicals and water pumps compared to water-cooled condensers. Both water-cooled and evaporative condensers can only cool to the outside wet bulb temperature, which is typically lower than the dry bulb temperature.

These condensers play a role in cooling the refrigeration system, consequently reducing electricity consumption. They offer improved efficiency and enhanced cooling capabilities compared to air-cooled condensers. Evaporative condensers consume less water than water-cooled counterparts with cooling towers, despite utilizing similar amounts for each refrigeration unit. The water system for evaporative condensers is entirely contained within the unit. As they are smaller and have fewer components, they are more cost-effective than water-cooled condensers. However, their planning and installation can be more complex than water and air-cooled condensers due to the water evaporating into the air during operation.

2. Theoretical model and methodology

The 3D Navier-Stokes approach via ANSYS simulated the airflow, dehumidification, and condensation processes within a room. This simulation involved calculations related to interior conditions, such as temperature, velocity, and humidity. Additionally, it evaluated the turbulent flow emanating from the room's duct outlet and accounted for the non-uniform heat flow originating from the walls. The experimental model underwent numerical solution using CFD (Computational Fluid Dynamics) software fluent within ANSYS 22 R1. This approach, based on vectors, resolves conservation equations for mass, momentum, energy, and species in stable three-dimensional flows.

2.1. Governing equations

The flow and energy equations are derived from the fundamental equations of fluid dynamics, namely continuity, momentum, and energy equations. The Navier-Stokes equations specifically describe the motion of fluids and are often likened to Newton's second law of motion applied to fluids.

$$\rho\left(\frac{\partial u}{\partial t}+u\cdot\nabla\mathrm{u}\right)=-\nabla p+\nabla.\left(\mu(\nabla u+(\nabla u)^{T})-\frac{2}{3}\mu(\nabla.u)\mathrm{I}\right)+F) \tag{3.1}$$

Where u is the fluid velocity, p is the fluid pressure, ρ is the fluid density, and μ is the fluid dynamic viscosity. The different terms correspond to the inertial forces:

(1) = $\rho\left(\frac{\partial u}{\partial t}+u\cdot\nabla\mathrm{u}\right)$, pressure forces

(2) = $-\nabla p$, viscous forces

(3) = $\nabla.\left(\mu(\nabla u+(\nabla u)^{T})-\frac{2}{3}\mu(\nabla.u)\mathrm{I}\right)$,

and the external forces applied to the fluid (4) = F.

2.1.1. Mass conservation equation:

$$\frac{\partial}{\partial x}(\rho u)+\frac{\partial}{\partial y}(\rho v)+\frac{\partial}{\partial z}(\rho w)=0 \tag{3.2}$$

2.1.2. Momentum conservation equations

The direction of the X-axis (U-momentum):

$$\frac{\partial}{\partial x}(\rho UU)+\frac{\partial}{\partial y}(\rho UV)+\frac{\partial}{\partial z}(\rho UW)=\frac{\partial}{\partial x}\left(\mu\frac{\partial U}{\partial x}\right)+\frac{\partial}{\partial y}\left(\mu\frac{\partial U}{\partial y}\right)+\frac{\partial}{\partial z}\left(\mu\frac{\partial U}{\partial z}\right)+\ \frac{1}{3}\frac{\partial}{\partial x}\left[\mu(\frac{\partial U}{\partial x}+\frac{\partial U}{\partial y}+\frac{\partial U}{\partial z})\right]= \tag{3.3}$$

The direction of the Y-axis (V momentum):

$$\frac{\partial}{\partial x}(\rho UV)+\frac{\partial}{\partial y}(\rho VV)+\frac{\partial}{\partial z}(\rho VW)=\frac{\partial}{\partial x}\left(\mu\frac{\partial V}{\partial x}\right)+\frac{\partial}{\partial y}\left(\mu\frac{\partial V}{\partial y}\right)+\frac{\partial}{\partial z}\left(\mu\frac{\partial V}{\partial z}\right)+\ \frac{1}{3}\frac{\partial}{\partial y}\left[\mu(\frac{\partial U}{\partial x}+\frac{\partial U}{\partial y}+\frac{\partial U}{\partial z})\right] \tag{3.4}$$

The direction of the Z-axis (W momentum):

$$\frac{\partial}{\partial x}(\rho UW)+\frac{\partial}{\partial y}(\rho VW)+\frac{\partial}{\partial z}(\rho WW)=\frac{\partial}{\partial x}\left(\mu\frac{\partial W}{\partial x}\right)+\frac{\partial}{\partial y}\left(\mu\frac{\partial W}{\partial y}\right)+\frac{\partial}{\partial z}\left(\mu\frac{\partial W}{\partial z}\right)+\ \frac{1}{3}\frac{\partial}{\partial w}\left[\mu(\frac{\partial U}{\partial x}+\frac{\partial U}{\partial y}+\frac{\partial U}{\partial z})\right] \tag{3.5}$$

(μ) = fluid viscosity of dynamic. Replacing U, V, and W by the time-mean and fluctuating components and assuming a pressure expression that is comparable to integrating and averaging with time.

2.1.3. Energy conservation equation

$$\frac{\partial}{\partial x}(\rho\bar{T})+\frac{\partial}{\partial y}(\rho V\bar{T})+\frac{\partial}{\partial z}(\rho W\bar{T})=\frac{\partial}{\partial x}\left(\Gamma\frac{\partial\bar{T}}{\partial x}\right)+\frac{\partial}{\partial y}\left(\Gamma\frac{\partial\bar{T}}{\partial y}\right)+\frac{\partial}{\partial z}\left(\Gamma\frac{\partial\bar{T}}{\partial z}\right)+S_{T} \tag{3.6}$$

2.2. The species concentration equation

$$\frac{\partial}{\partial x}(\rho \mathrm{uc}) + \frac{\partial}{\partial y}(\rho \mathrm{vc}) + \frac{\partial}{\partial z}(\rho \mathrm{wc}) = \frac{\partial}{\partial x}\left(\Gamma \frac{\partial \mathrm{c}}{\partial x}\right) + \frac{\partial}{\partial y}\left(\Gamma \frac{\partial \mathrm{c}}{\partial y}\right) + \frac{\partial}{\partial z}\left(\Gamma \frac{\partial \mathrm{c}}{\partial z}\right) + \frac{\partial}{\partial x}(-\rho \overline{\acute{u}\mathrm{c}'}) + \frac{\partial}{\partial y}(-\rho \bar{\acute{v}}\bar{\mathrm{c}}') + \frac{\partial}{\partial z}(-\rho \bar{\acute{w}}\bar{\mathrm{c}}') + S_T \quad (3.7)$$

The terms −ρu′c′, −ρv′c′, and −ρw′c′ are the turbulent diffusion fluxes, J.C.

2.2.1. Species transport equations

$$\frac{\partial}{\partial t}(\rho Y_i) + \nabla \cdot (\rho \vec{u} Y_i) = -\nabla \cdot \vec{J_i} + R_i + S_i \quad (3.8)$$

2.2.2. Mass diffusion in turbulent flows

$$\vec{J_i} = -\left(\rho D_{i,m} + \frac{\mu_t}{SC_t}\right) + \nabla Y_i - D_{T,i}\frac{\nabla T}{T} \quad (3.9)$$

2.2.3. Treatment of species transport in the energy equation

$$\frac{\partial(\rho \emptyset)}{\partial t} + \nabla \cdot (\rho \emptyset u) = \nabla.(\Gamma \nabla \emptyset) + S_\emptyset \quad (3.10)$$

$[\frac{\partial(\rho \emptyset)}{\partial t}]$=Temporal Term, $[\nabla \cdot (\rho \emptyset u)]$=Convective Term,

$[\nabla.(\Gamma \nabla \emptyset)]$=Diffusion Term,$[S_\emptyset]$=Source Term

2.3. Transport equations for the standard (k-ε)

$$\frac{\partial}{\partial x_j}(\rho k u_i) = \frac{\partial}{\partial x_j}\left(\mu + \frac{\mu_t}{\sigma_k}\right)\frac{\partial k}{\partial x_j} + G_K + G_b - \rho\varepsilon - Y_M + S_T \quad (3.11)$$

$$\frac{\partial}{\partial x_i}(\rho \varepsilon u_i) = \frac{\partial}{\partial x_j}\left[\left(\mu + \frac{\mu_t}{\sigma_\varepsilon}\right)\frac{\partial \varepsilon}{\partial x_j}\right] + C_{1\varepsilon}\frac{\varepsilon}{k}(G_K + c_{3\varepsilon}G_b) - c_{2\varepsilon}\rho\frac{\varepsilon^2}{k} + S_\varepsilon \quad (3.12)$$

Where: (G_k): Mean velocity gradients cause turbulence kinetic energy creation.

(G_b): Is turbulence kinetic energy.

(Y_M): Modeling incompressible flows ignores the effect of variable dilatation incompressible turbulence on the total dissipation rate.

(C_{1e}), (C_{2e}), and (C_{3e}) are constants.

(σ_k), (σ_e) are turbulent Prandtl numbers for k and ε.

(C_{1e}), (C_{2e}), (σ_k), and (σ_e) constant models have the following default values.

C_{1e} = 1.44; C_{2e} = 1.92; σ_k = 0.09; σ_e = 1.3.

(S_k), (Se) are user-defined source terms [25].

2.3.1. Modeling turbulent production in the *k*-models

$$G_K = -\rho\overline{u_i' u_j'}\frac{\partial u_i}{\partial x_i} = \mu_t\left(\frac{\partial U_i}{\partial xj} + \frac{\partial U_j}{\partial x_i}\right) \quad , \quad \mathrm{G} = \mu_t \, \mathrm{S}^{\wedge 2} \quad (3.13)$$

$$S \equiv \sqrt{2 S_{ij} Sij} \quad (3.14)$$

$$G_b = \beta g_i \frac{\mu_t}{pr_t}\frac{\partial T}{\partial x_i} \quad (3.15)$$

g_i: Component of the gravitational vector in i-direction

β: Thermal expansion coefficient

2.3.2. Effects of buoyancy on turbulence in the *k*-models

When a non-zero gravity field and temperature gradient are present, the k-epsilon (k-) models in Fluent software account for the generation of 'k' due to buoyancy in Equation 3.11 and the corresponding contribution to the production of 'epsilon' in Equation 3.12. The generation of turbulence due to buoyancy is given by:

$$G_b = \beta g_i \frac{\mu_t}{pr_t} \frac{\partial T}{\partial x_i} \ , \quad (3.16)$$

Where 〖Pr〗_t is the turbulent Prandtl number for energy, and g is the component of the gravitational vector in the I th direction. For the standard (k-ε) models, the default value of 〖Pr〗_t is 0.85. The coefficient of thermal expansion is defined as:

$$\beta = -\frac{1}{\rho}(\frac{\partial \rho}{\partial T})_P \quad (3.17)$$

2.4. Numerical procedure

2.4.1. The structure of ANSYS Fluent 22R1

ANSYS Fluent consists of four software modules that take geometry and mesh and pass the information required to perform a CFD analysis, as shown in Fig. 1.

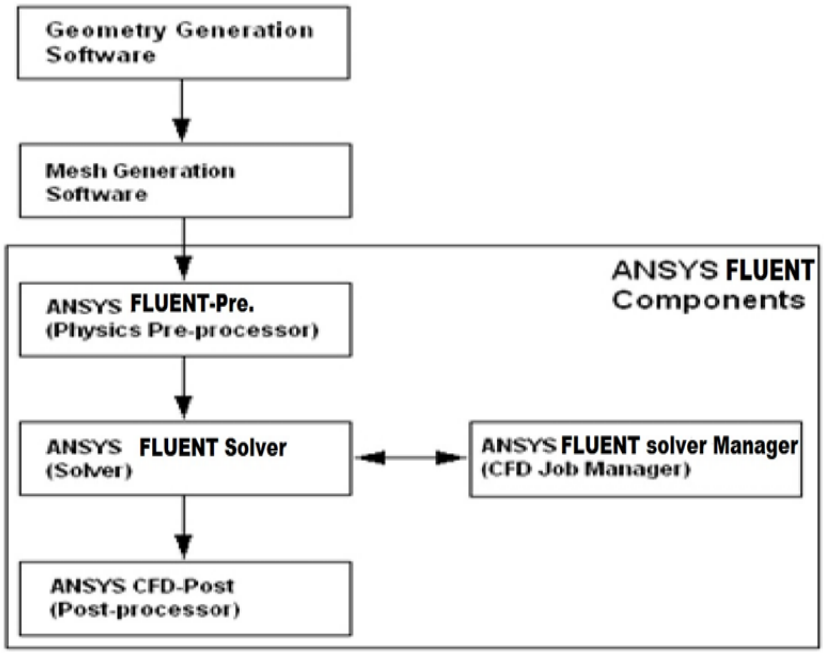

Figure 1. The structure of ANSYS Fluent; 1–Preprocessor, 2–Solver, 3–Post processor [24]

2.5. Model description by using ANSYS 22/R1

The tester room at Al Najaf Hospital measures 4m in length, 3m in width, and 2.5m in height. The construction features walls made of hollow concrete blocks, and the roof consists of galvanized Kirby corrugated iron, with an internal secondary ceiling made of gypsum board. Conditioned air is provided through an inner rectangular supply air duct located on the northern wall. The measuring duct, measuring 2m in length, 0.3m in width, and 0.6m in height, comprises three slots; slot 1 delivers air at a velocity of 4m/s with a temperature of 28℃ from the evaporative air cooler device, slot 3 supplies air at a velocity of 1.5m/s and a temperature of 16°C from the air conditioner, and slot 2 is a mix of the two airflow streams. The room's geometry was designed using ANSYS Fluent 22/R1. Figures 2 and 3 illustrate the room's dimensions and layout. Designing the interior and exterior walls posed the most significant challenges during modeling. The roof was exposed to daily environmental fluctuations, especially in May, June, September, and October, which affected both the outer and inner walls. These fluctuations in daily temperatures led to changes in the results within the room, such as increased inner wall temperatures and variations in relative humidity and temperature levels.

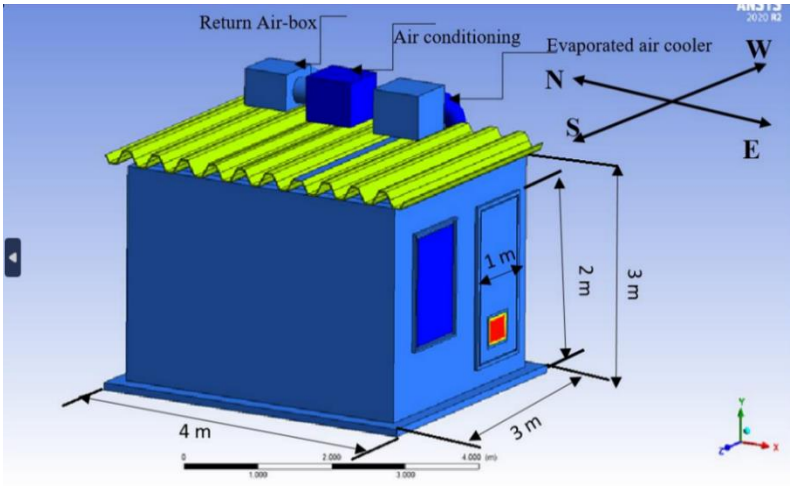

Figure 2. Geometry of the designed room by ANSYS Fluent

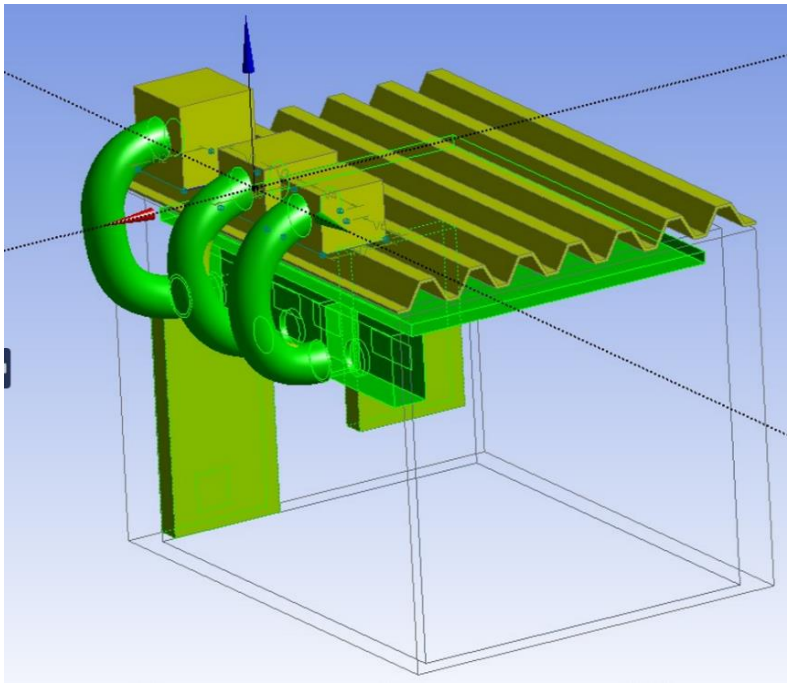

Figure 3. Geometry of the designed room contents by ANSYS Fluent

Moreover, a return air duct enables the room's air to circulate back to the air conditioner, enhancing air quality and producing clean water. The heat transfer boundary conditions for all walls, except the floor, are adjusted to account for the varying climatic conditions. The tester room features a single door located at a height of two meters from the base, measuring one meter in width, along with two windows positioned at an elevation of 1.5 meters and with a width of 1 meter.

2.5.1. Mesh design

While assessing grid dependency, the conclusions' accuracy was verified by increasing network density. The air ducts located along the north wall and positioned below the ceiling underwent testing to analyze primary flow or heat distribution. Figure 5 illustrates the incremental mesh refinement in these zones and their surroundings until achieving network independence. Irregular grid layouts were implemented in complex sections to tackle the challenges posed by 3D physics, while standard grid layouts were utilized in geometric areas due to limitations in cube and microscopic sizes. Despite the considerable space in the room allowing for a restricted grid, which might prolong the precision of findings for several days or more in each case, it does not compromise the accuracy.

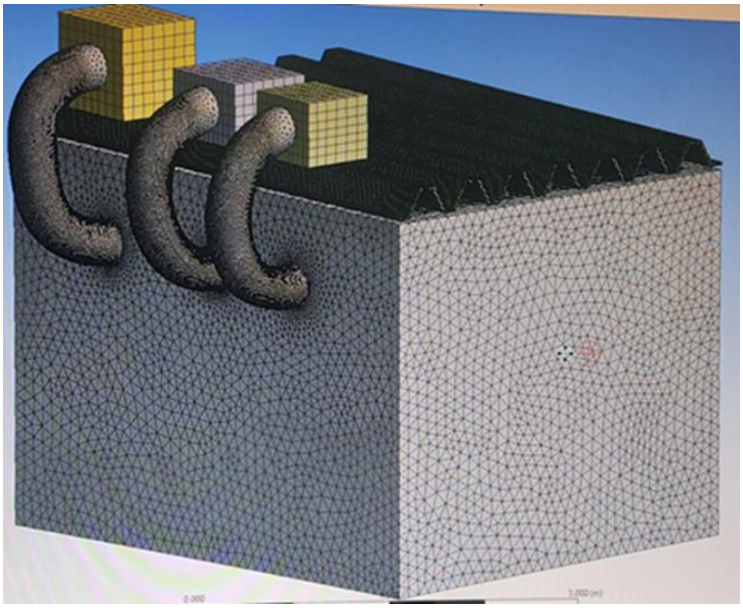

Figure 4. View grid of the tester room

During the 3D modeling process using the ANSYS program, diverse grid structures were utilized, incorporating triangular cells in complex geometric regions and quadrilaterals, tetrahedral, and hexahedral cells in cubes, geometric volumes, polyhedrons, pyramids, or wedges. The choice of mesh type relied on the specific application. For this study, a combination of tetrahedral and hexahedral grids was employed, as shown in Fig 6.

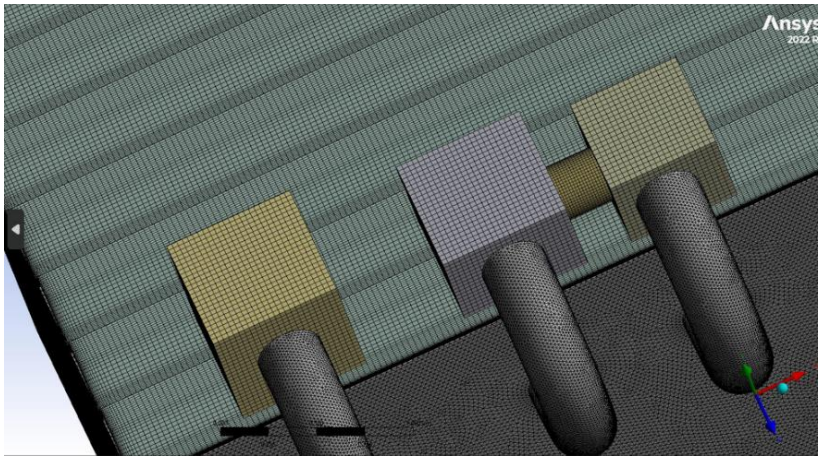

Figure 5. Mesh types in the present work

2.6. Thermal comfort assessment

The Predicted Mean Vote (PMV) index predicts the average response of a substantial number of individuals on a 7-point scale representing thermal sensation, ranging from +3 (hot) to -3 (cold), with 0 indicating a neutral state. ANSI/ASHRAE Standard 55 defines an occupant-controlled naturally conditioned space as an environment where occupants primarily adjust thermal conditions using openings in the building's envelope. The empirical equation for assessing human exposure over 3 hours, converted to S.I. units, is represented by:

$$PMV=0.243T+0.278PV-6.802 \quad (3.31a)$$

$$Pv=RH\times P\_s \quad (3.31b)$$

$$Ps=\exp[25.317-5144/(T+273)]/1000 \quad (3.31c)$$

These equations calculate the PMV and relate to the ASHRAE thermal sensation scale, which spans from -3 to 3 as shown in Figure 6.

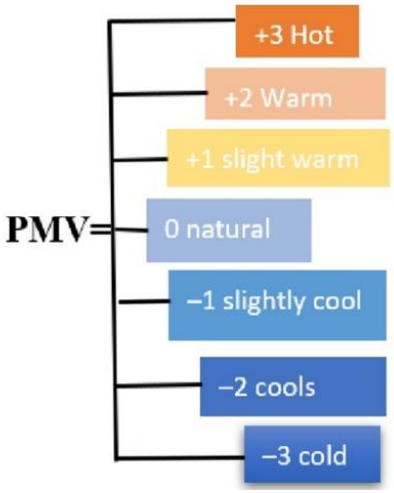

Figure 6. Schematic of a typical evaporator coil

2.7. The cooling process

The cooling system involves two primary heat transfer methods. Firstly, in the evaporative cooler, water evaporation cools and humidifies the hot outside air. This process is governed by the convective heat transfer coefficient and the temperature difference between the exterior air and the evaporative cooler. Secondly, the air conditioning device cools and dehumidifies the mixed return air from the test room, facilitating heat transfer. The heat transmission in this process is influenced by the temperature difference between the outside air and the air conditioning unit, along with the convective heat transfer coefficient.

Water evaporation humidifies the outside air in the evaporative cooler, regulated by the convective mass transfer coefficient and the humidity difference between the room air and the evaporative cooler. In the air conditioning unit, the process of dehumidifying indoor air involves mass transfer, which is affected by the convective mass transfer coefficient and the humidity difference between the outside air and the air conditioning unit, as depicted in Figure 7.

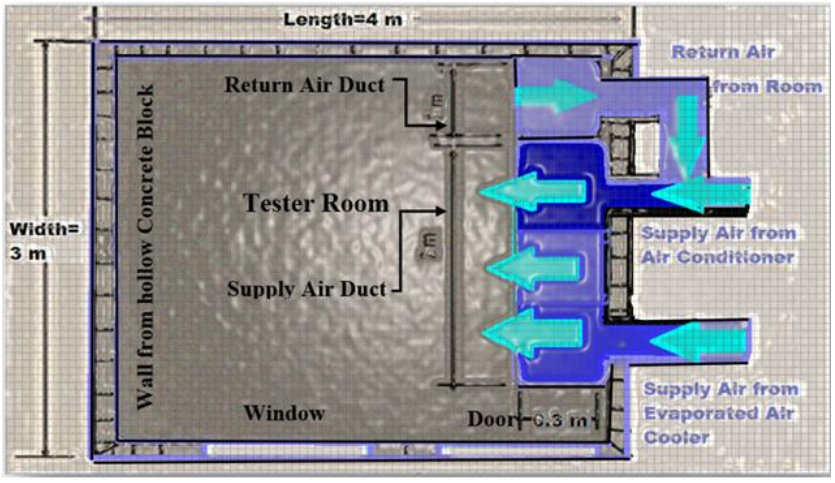

Figure 7. Schematic of testing room top view (imaginary)

3. Verification cases

3.1. Verification case 1

In this study, as a first step, the appropriateness of the ANSYS 22 R1 program is validated against the results reported by [21]. The governing equations (mass conservation, momentum, energy, and concentration) for turbulent airflow inside a room with dimensions of 6 meters in length, 4 meters in width, and 2.4 meters in height are generated, aligning with the dimensions used in the aforementioned researcher's work. The flowing

air was contaminated with particles at varying concentrations. A model akin to the one presented in [21] is constructed using the ANSYS 17 program, and the aforementioned governing equations are solved using the same program, ANSYS/CFD/CFX-17.

The current model closely resembles Model Number 1, which operates exclusively with an evaporative air cooler, enabling a detailed analysis of its thermal performance. The primary objective of this verification study is to ensure the accuracy and reliability of the existing code. Table 1 provides a comprehensive comparison of the boundary conditions for both the researcher's case and Verification case 1, thoroughly evaluating the data inputs for both studies.

$$percentage\ error\ (e) = \frac{x_f - x_s}{x_f} \times 100$$

Where, x_f= Previous value

x_s= Present value

Figures 8 and 9 present the diagrams and meshes used for both the researcher's case and verification case 1, both focusing on the model's operation with evaporative air cooling only. Figures 10 and 11 showcase the contours of both models. Examination of the air velocity contours in the vertical plane (Y=1.3) and the horizontal plane (Z=2) revealed a minimum of 92% agreement between the researcher's model and verification case 1.

Any discrepancies between the two results are then quantified. In the horizontal plane, the researcher's air velocity range is 0–1.00 m/s, while verification case 1 exhibits a range of 0–0.99 m/s. In the vertical plane, the researcher's air velocity range spans 0–3.2 m/s, whereas verification case 1 shows an air velocity range of 0–3.02 m/s. These differences indicate an acceptable level of convergence between the two sets of results. To comprehensively compare both research types, the results were plotted in Chart 1, and their differences were calculated. The maximum and minimum percentage error values are tabulated in Table 2. It's worth noting that the generally accepted range of difference falls between 10% and 20%, as commonly reported in indoor airflow measurements and simulations, as summarized in Table 3. To delve deeper into this analysis, specific points in Figure 12 were examined, particularly near the E.C. levels and the surrounding area.

Table 1. Values of boundary conditions derived from researcher case [1] and compared to verification case 1

Boundary condition	Researcher case [l]	Verification case l
Drawing	ANSYS CFX-17/DM (3D)	ANSYS -Fluent-17/DM (3D
Meshing	Mesh model/ tetrahedral elements	ANSYS/Mesh/hexagonal element
Nodes	-	29389
Elements	-	54895
Simulation b	ANSYS/ CFO/ Fluent	ANSYS/ CFO/ Fluent
Energy	On	On
Viscous	Turbulent model	Realizable k-e, Standard
Species	Relative humidity	Species Transport
Inlet velocity	3.2 m/s	3.2 m/s
Inlet temp.	T-19.1 °C	T-19.1 °C
Water vapor concentration	0.011	0.011
Pressure-outlet	0 bar	0 bar
Walls	Isolated	Isolated

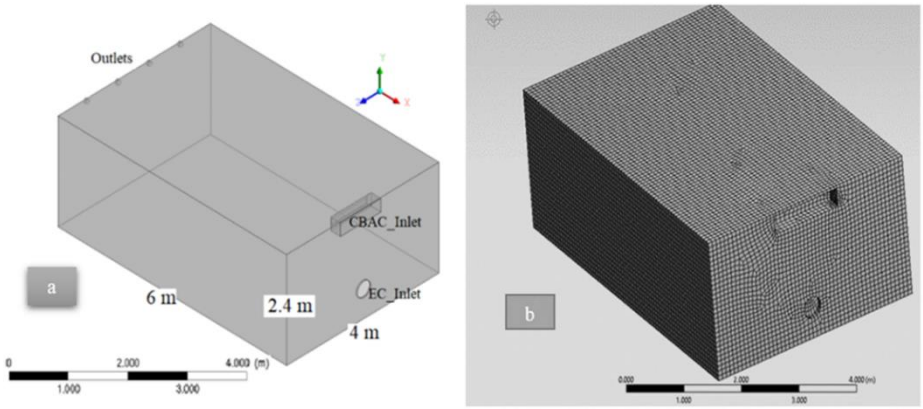

Figure 8. (a) Design room and (b) Mesh drawing a researcher [26]

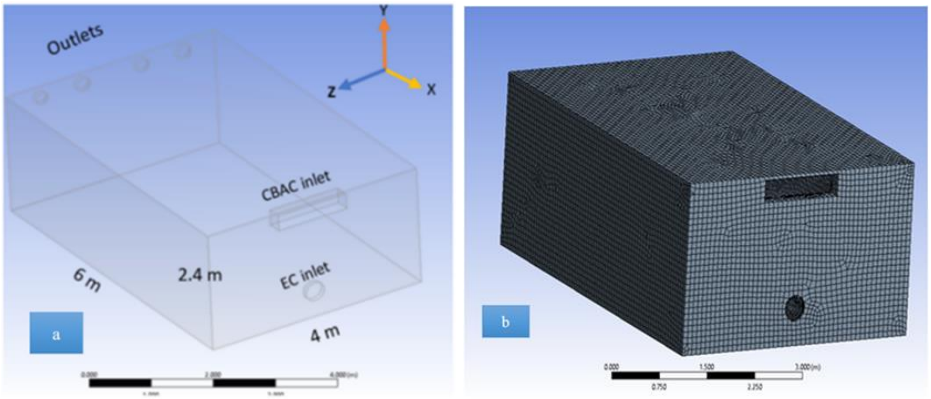

Figure 9. (a) Design modeler (b) Mesh drawing created by verification case 1

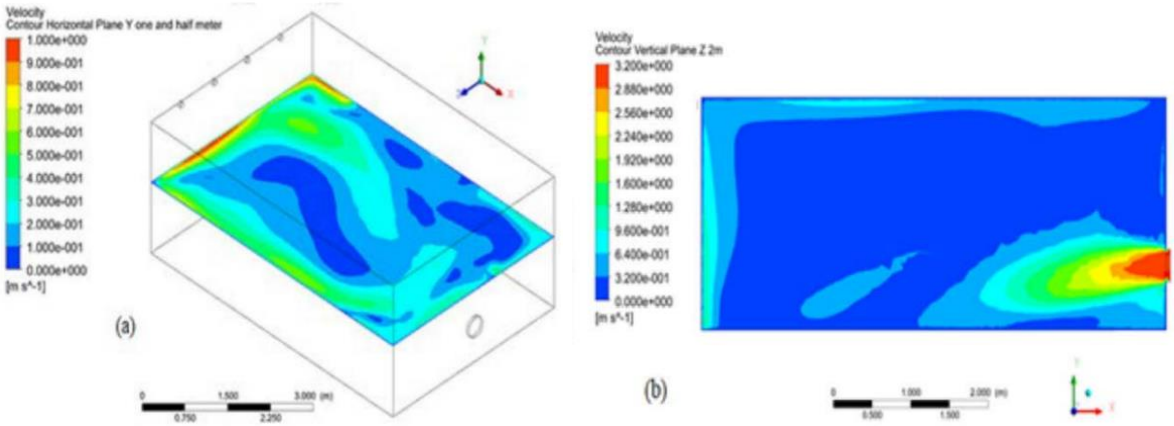

Figure 10. (a) Velocity contours horizontal plane 1.5 m (b) Velocity contours vertical plane 2 m for a researcher [26]

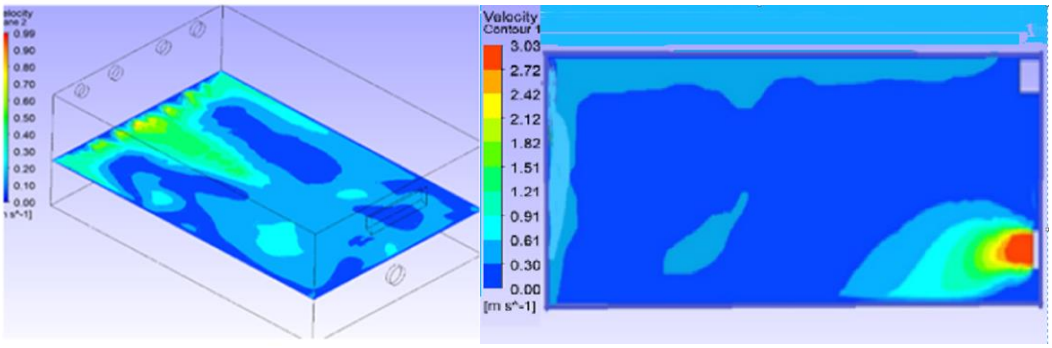

Figure 11. (a) Velocity contours horizontal plane 1.5 m (b) Velocity contours vertical plane 2 m for verification case 1

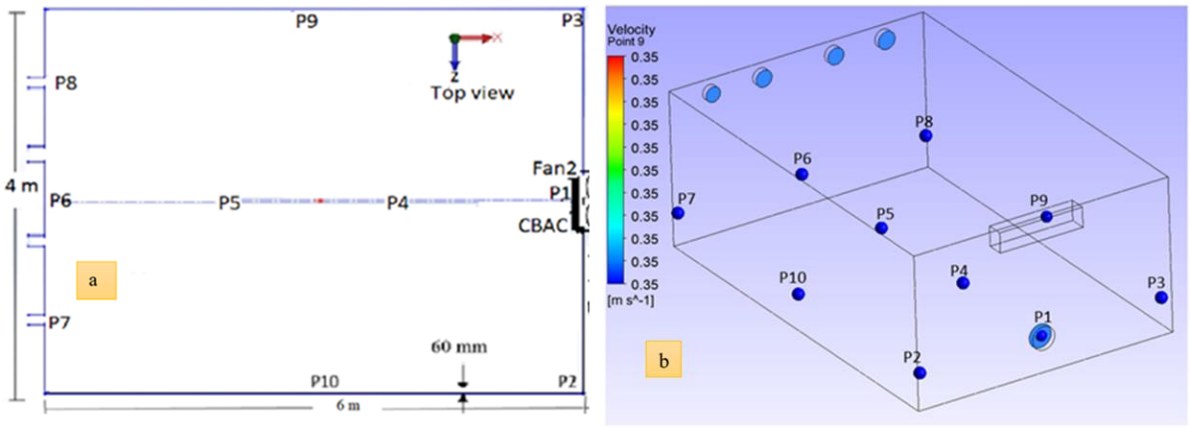

Figure 12. Positions of points at different locations inside E.C. a) researcher case [26] and b) verification case 1

Table 2. Measured and numerical values of air velocities and temperatures at selected domain points for the primary case [21]

$(Cooler)_{researcher1}$	Temperature (°C)				Relative humidity (RHI				Airspeed (m/s)	
	P1	P4	P5	Exit	P1	P4	P5	Exit	Inlet	Exit
EC	19.1	21.4	21.1	22	97.3	98.7	981	92.9	3.2	3.3
$(Cooler)_{current\ work}$	Temperature (°C)				Relative humidity (RH)				Airspeed (m/s)	
	P1	P4	P5	Exit	P1	P4	P5	Exit	Inlet	Exit
EC	19	21.1	216	22.8	983	98.4	95.7	954	3.2	3.3

Table 3. The comparison depends on an error in the results

Points	P1	P4	5	Exit
Error % T_R with $T_{C.W}$	0.5	1.4	2.4	3.6
Error % RH_R with $RH_{C.W}$	1	0.3	2.4	2.7

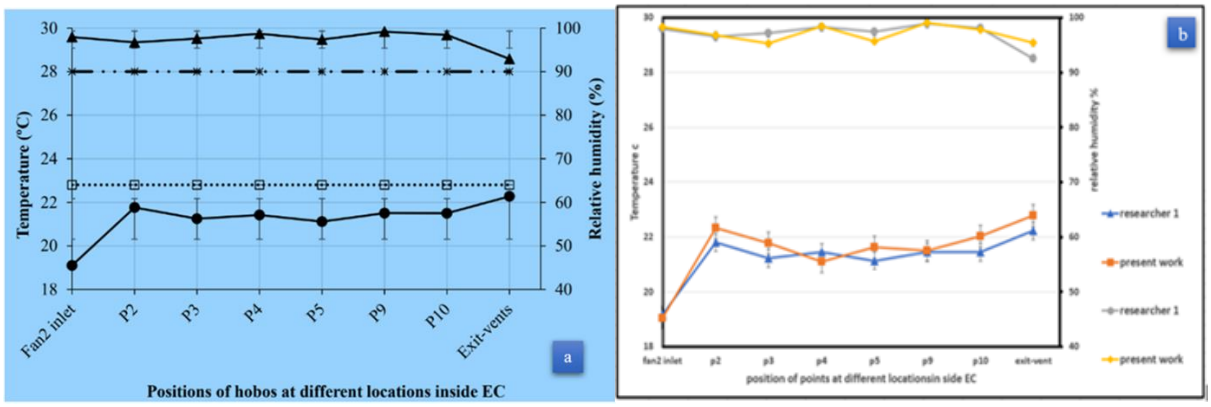

Chart 1. Comparison of measured and numerical values of temperature and relative humidity of the domain points a) researcher [26] and b) verification case 1

3.2. Verification case 2

A verification study was conducted for case 2, previously investigated by Begdouri et al. [22]. The analysis utilized the ANSYS-17/CFD/Fluent program, focusing on the room's thermal performance by examining temperature, velocity, and relative humidity distributions. In this configuration, the room was conditioned solely by the window-type air conditioner. The dimensions of this designed room were chosen to match the model studied by the researcher [27], who conducted numerical and experimental studies using the CFD/Fluent-FIDAP program. The specified dimensions for this case were 4.8 x 4 x 2.7 cubic meters. The detailed boundary conditions for case 2, examined by the researcher, and verification case 2 are presented in Table 4. Additionally,

plane views of both rooms are depicted in Figures 13 and 14. Validation was determined by comparing the researcher's contour with the results of the present study. For comparison, the boundary conditions for case 2, as studied by the researcher, and the verification case 2 are detailed in Table 4.

Table 4. Values of boundary conditions derived from researcher case [2] and compared to verification case 2

Boundary condition	Researcher case [2]	Verification case 2
Drawing	Fluent/GAMBIT (2D/3D)	ANSYS 17/DM 2D/3D
Mesh	mesh model	ANSYS/Mesh
Nodes	-	107190
Elements	-	491301
Simulation	ANSYS/ CFO,' Fluent	ANSYS/ CFO/ Fluent
Energy	On	On
Viscous	K-ε SST model	Realizable K-e, Standard
Species	Relative Humidity	Species Transport
Inlet velocity	3.50 m/s	3.50 m/s
Inlet tem	T=19 °C	T=19 °C
Water vapor concentration	0.01	0.01
Pressure-outlet	0 bar	0 bar
Walls	T=24 °C	T=24 °C
Person	T-34 °C /Flux=5E 6	T-34 °C /Flux=5E-6
Light	Flux=50 w/m^2	Flux=50 w/m^2

Figures 13 and 14 illustrate the 3D and 2D design models and vector planes studied for both the researcher's case and Verification Case 2.

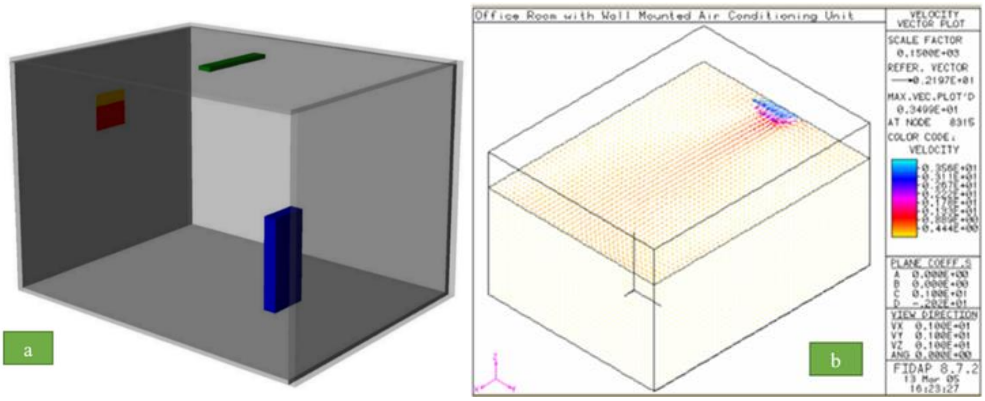

Figure 13. The drawing created by (a) design modeler 3D and (b) velocity vector plane for a researcher [22]

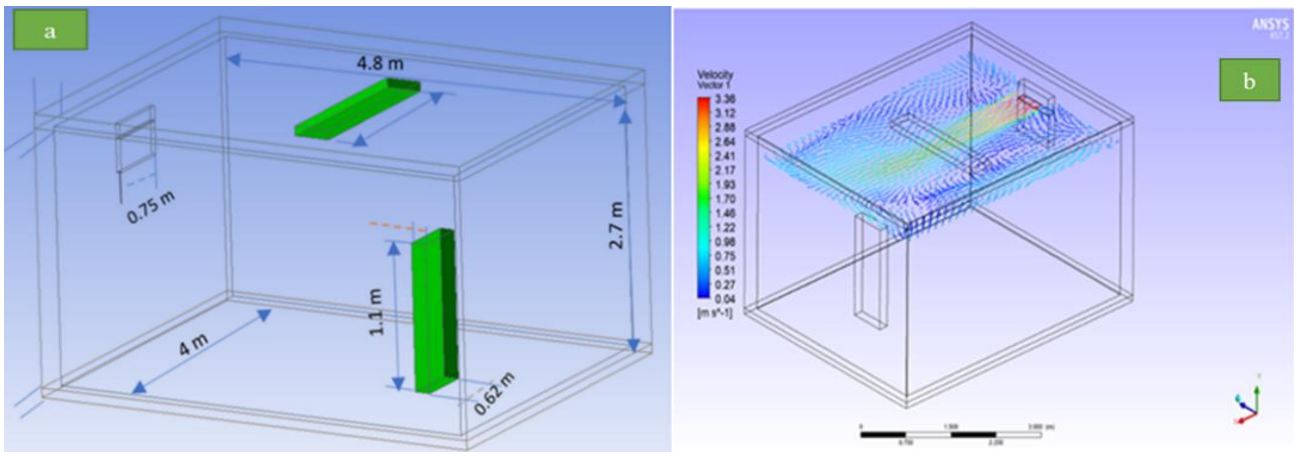

Figure 14. The drawing created by (a) design modeler 3D and (b) vector plane for a verification case [22]

Table 5. Measured and numerical values of air velocities and temperatures at selected domain points for the primary case [22]

$V_{Research}$	$V_{Verification\ Case\ 2}$	$T_{Research}$	$T_{Verification\ Case\ 2}$
4.35	4.62	20.9	19
3.8	3.75	24.8	23.1
3.26	3.46	28.7	28
2.72	2.89	32.6	32
1.63	1.73	40.4	38
1.09	1.15	44.3	41
0.54	0.87	48	42

Table 6. Comparison depends on an error in the results

Error %	Error % V_R with V_{c-w}	Error % T_R with T_{c-w}
1.	6.2	9
2.	1.3	6.8
3.	6.13	2.4
4.	6.25	1.8
5.	6.13	5.9
6.	5.5	7.4
7.	6.11	12.5

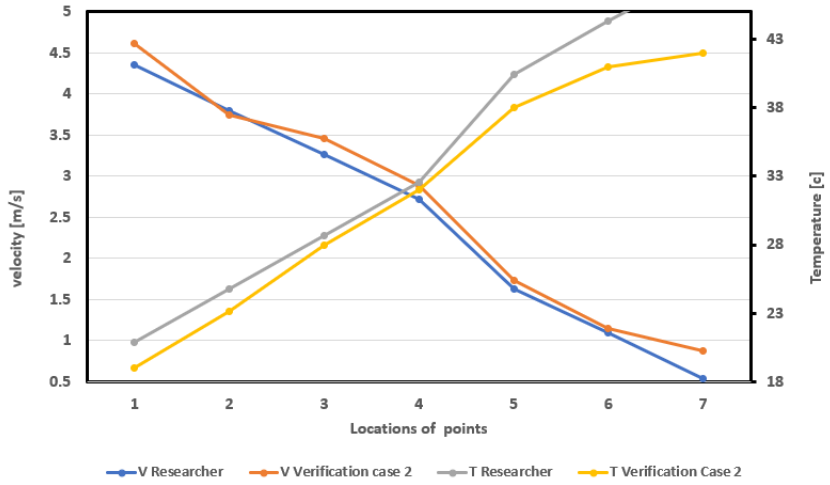

Chart 2. Comparison of measured and numerical values of temperature and velocity of the domain points a) researcher [22] and verification case 2

4. Grid independence study

Mesh quality significantly impacts the accuracy and stability of numerical computations. If there are issues with grid quality, ANSYS will generate a warning message in the console, highlighting problems identified with the mesh. The geometry was created using ANSYS Design Modeler (DM) within the ANSYS program and later transferred to ANSYS Meshing for the meshing process. Various types of meshes were employed to achieve the necessary mesh quality that ensures accurate resolution for solving the problem.

For each type of mesh, there are three stages of mesh size: course mesh, medium, and fine mesh. As Table 7 shows, Mesh 2 is the best in the current study when transferring from Mesh 6 to Mesh 7 because Mesh 6 has less error.

Table 7. Convergence between Mesh 1 and Mesh 2 results

Number of points	Positions of points	Mesh 1		Mesh 2		Mesh 3		Mesh 4		Mesh 5	
	(X,Y,Z)	Temp. [k]	Vel. [m/s]	Temp. [k]	Vel. [m/s]	Temp. [k]	Vel. [m/s]	Temp. [k]	Vel. [m/s]	Temp. [k]	Vel. [m/s]
	Element size (m)	0.2		0.1		0.08		0.05		0.03	
	# of divisions	10		10		10		10		10	
	Node	539627		635147		712721		2317906		3431703	
	Element	1533743		1944079		2336815		5145462		17448550	
	Skewness	0.74939		0.74954		0.74874		0.77997		0.76469	
P1	(2,2,2,3,2)	300.60	1.23	300.83	1.20	300.80	1.29	301.50	1.33	302.90	1.44
P2	(2,2,1,2,4)	300.86	0.19	301.11	0.17	301.16	0.18	301.79	0.16	303.27	0.16
P3	(2,2,1,8,1, 4)	300.86	0.14	301.07	0.21	301.10	0.21	301.78	0.13	303.24	0.29
P4	(3,2,1,6,1)	300.90	0.26	301.15	0.21	301.18	0.21	301.84	0.23	303.35	0.12
P5	(3,2,2,4,2, 3)	300.81	0.27	301.04	0.27	301.06	0.30	301.76	0.32	303.20	0.39
P6	(3,1,2,1,6)	300.87	0.16	301.10	0.15	301.13	0.15	301.85	0.20	303.30	0.20
P7	(1,2,3,2,8)	301.10	3.50	301.15	3.50	301.15	3.50	301.26	3.50	301.70	3.51
P8	(1,1,8,1,1)	300.90	0.25	301.20	0.25	301.17	0.27	301.84	0.24	303.24	0.46
P9	(1,1,8,1,1)	300.93	0.47	301.16	0.40	301.18	0.45	301.84	0.78	303.29	0.77
	Average values	300.87	0.72	301.09	0.71	301.10	0.73	301.72	0.77	303.05	0.82

5. Theoretical results and discussions

This chapter presents the findings of an extensive study conducted over five months from May to October 2021-2022. It investigates the impact of various parameters on the thermal comfort of a specially designed test room cooled by an evaporative air cooler and a window air conditioner. These parameters encompass relative humidity, air temperature, and air velocity. Comprehensive records of external variables were maintained to comprehend their influence on internal conditions. The analysis involved performing calculations using ANSYS 22/R1 software. The numerical results were obtained using the ANSYS 2022/R1 Species Transport software tool. These simulation studies are essential for validating the results, comparing them with experimental data, and presenting findings that explore the relationship between outdoor climate conditions

and the conditions within the conditioned room, considering factors such as temperature, air velocity, humidity, and weather conditions.

5.1. Analysis and study of the present case by using ANSYS 22/R1

The study involved utilizing the ANSYS 22/R1 Fluent program to operate both cooling systems. Various horizontal and vertical planes and lines were employed to assess specific locations in the room, as detailed in Table 8. These evaluations encompassed measuring relative humidity, temperature, and air velocity, as illustrated in Figure 15. Data collection was performed on the 14th day of four hot summer months (May, June, September, and October) at 1:30 p.m., and the results are depicted in Figures 16, 17, 18, and 25. Lines 1, 2, 9, and 10 were strategically positioned at specific heights and distances from the air supply slots of the EC and window AC. The most precise data readings were observed within specific elevations and lengths, showcased in Figures 3 to 10, highlighting differences in air temperature during the transition from summer to the beginning of winter, particularly noticeable in October and September. Near the air supply vent of the window air conditioner, as shown in Figures 16, 17, 20, 22, and 23, at a height range of 1.6 to 2 meters, there was a decrease in air temperature. The air velocity ranged from 1.25 to 2 m/s for the window air conditioner, while the evaporative air cooler demonstrated a higher velocity, approximately 4 m/s, resulting in cooler conditions near the air supply and relatively warmer conditions near the walls.

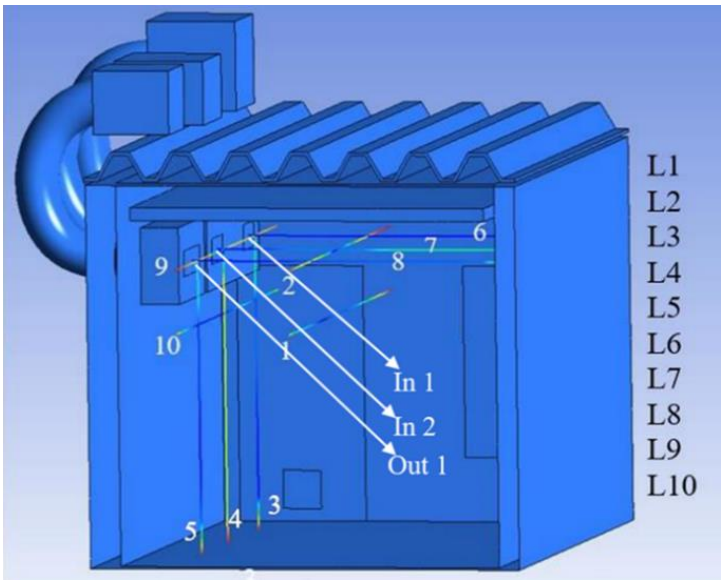

Figure 15. Locations of straight lines (horizontal and vertical) inside the room

Table 8. Position lines (horizontal and vertical) inside the room

Lines	X1 (m)	X2 (m)	Y1 (m)	Y2 (m)	Z1 (m)	Z2 (m)
1	0	4	1.6	1.6	1.65	1.65
2	0	4	2	2	1.65	1.65
3	0.85	0.85	0	2	2.5	2.5
4	2	2	0	2	2.5	2.5
5	3	3	2	2	2.5	2.5
6	0.85	0.85	2	2	2.5	0
7	2	3	2	2	2.5	0
8	3	3	2	2	2.5	0
9	0	4	2	2	2.5	2.5
10	0	4	1.6	1.6	2.5	2.5

Table 9. Comparison between temperatures of straight lines on the 14th day for four months

Lines	May 14th	June 14th	Sept 14th	Oct 14th
1	301.0	301.7	300.6	297.9
2	300.9	302.0	301.1	298.3
3	302.2	301.5	300.7	298.2
4	300.3	300.2	300.3	296.7
5	300.9	300.8	300.4	297.1
6	303.9	303.8	302.9	300.3
7	296.2	298.4	296.5	294.3
8	301.3	302.3	300.0	297.5
9	301.4	302.4	301.8	297.6
10	301.8	301.5	301.1	297.2
Average [K]	301.0	301.5	300.5	297.5
Ave/TH.[C]	28.0	28.5	27.5	24.5

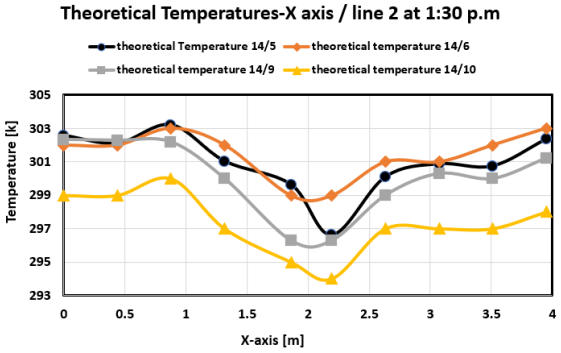

Chart 3. Temperatures four months 2.55 m

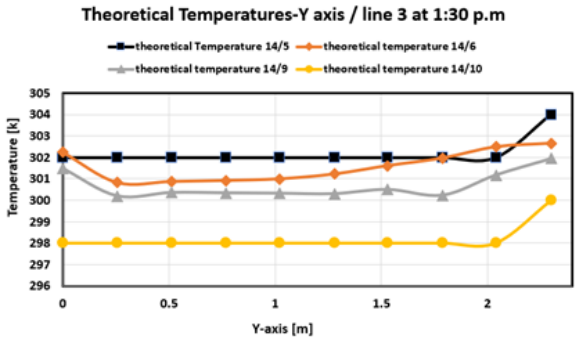

Chart 4. Temperatures four months at X=0.85 m, at Y=2 m, Z=1.65 m

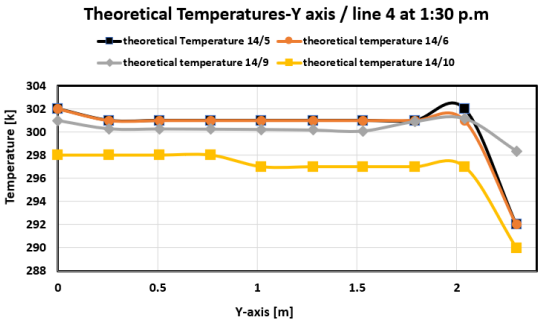

Chart 5. Temperatures for four months Z=2.55 m

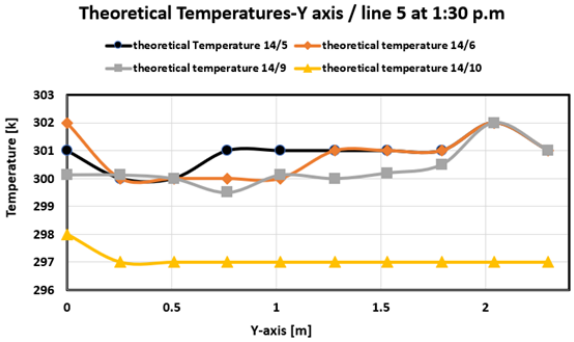

Chart 6. Temperatures for four months at X=3 m, at X=2 m, Z=2.55 m

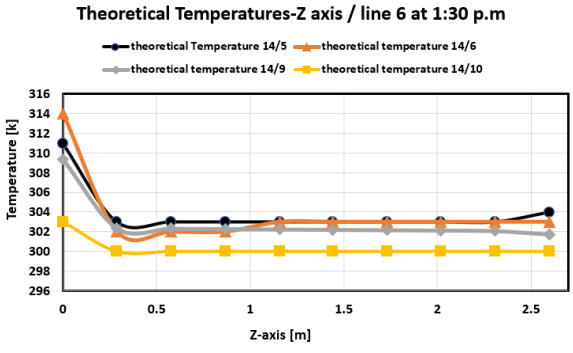

Chart 7. Temperatures for four months m, Y=2 m

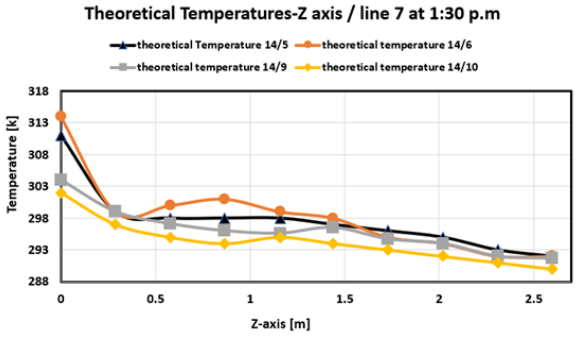

Chart 8. Temperatures for four months at X=2 at X=0.85 m, Y=2 m

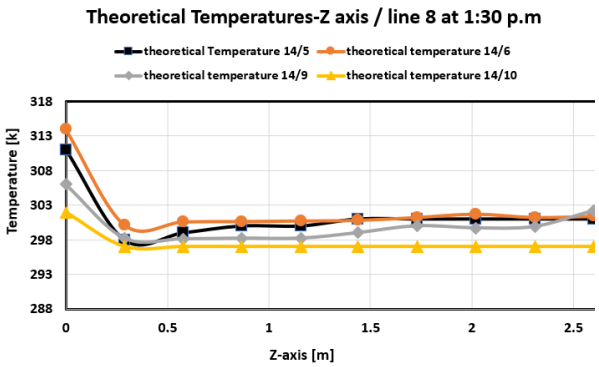

Chart 9. Temperatures for four months m, Y=2 m

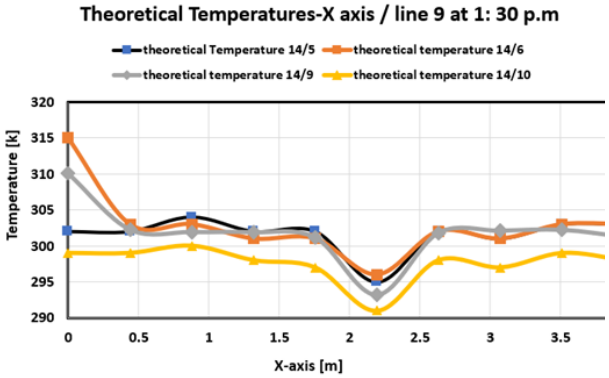

Chart 10. Temperatures for four months at Z=2.55 at X=3 m, Y=2 m

In Charts 11 to 20, variations in relative humidity are observed across four months: May, June, September, and October. These differences are most noticeable in September, corresponding to the changing external conditions associated with the onset of the autumn season. This external shift directly impacts the internal relative humidity levels within the room. The most significant relative humidity increase is noted near the air supply vent of the window-type air conditioner, particularly within the heights of Y=1.5 m to 2.5 m and within the Z=2 m to 2.5 m range. Conversely, relative humidity decreases as the cooler air moves closer to the room's walls.

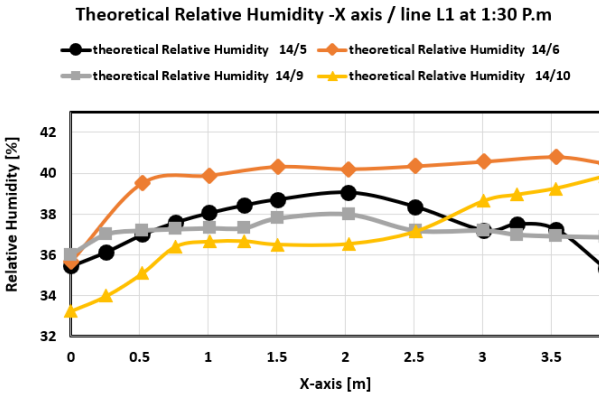

Chart 11. Relative humidity for four months at Z=1.65 m, Y=1.6 m

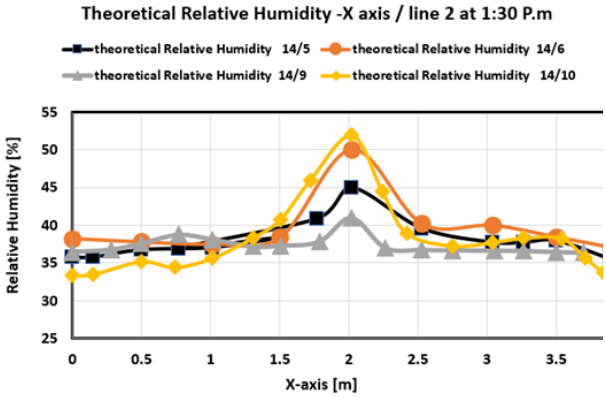

Chart 12. Relative humidity for four months at Z=1.65 m, Y=2 m

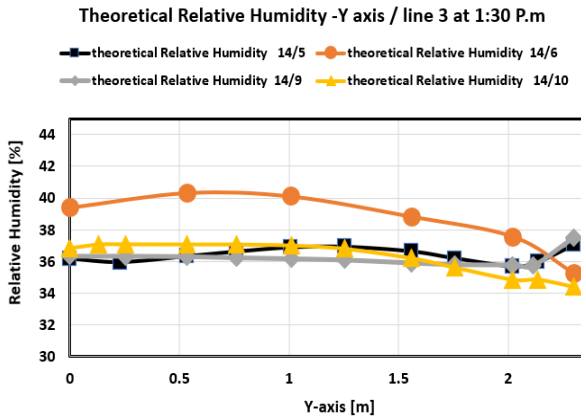

Chart 13. Relative humidity for four months at Z=2.5 m, X=0.85 m

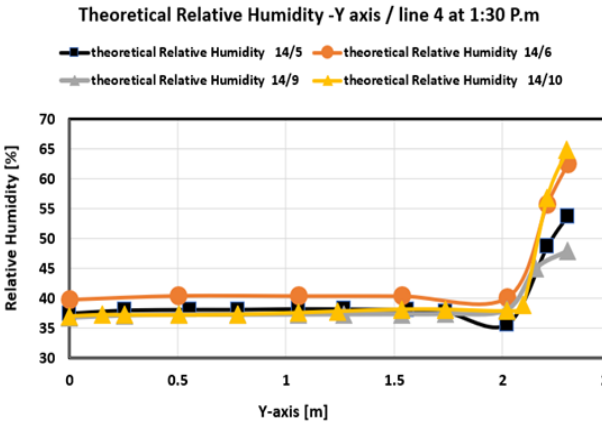

Chart 14. Relative humidity for four months at Z=2.5 m, X=2 m

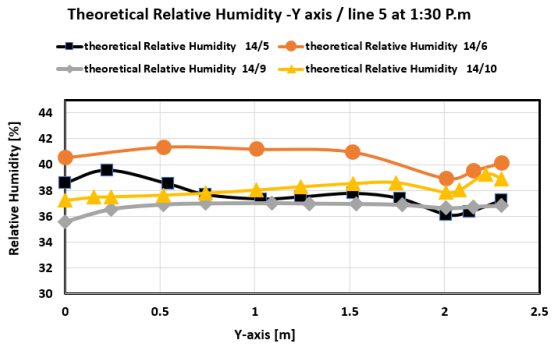

Chart 15. Relative humidity for four X=0.85 m

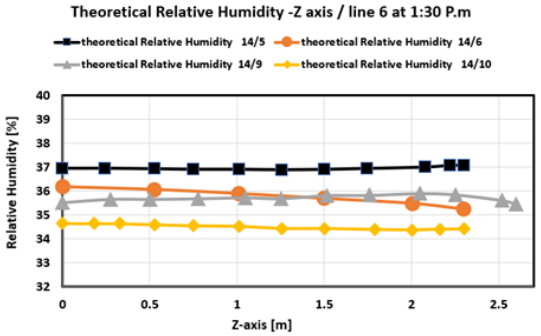

Chart 16. Relative humidity for four months at Y=2 m, months at Z=2.5 m, X=3 m

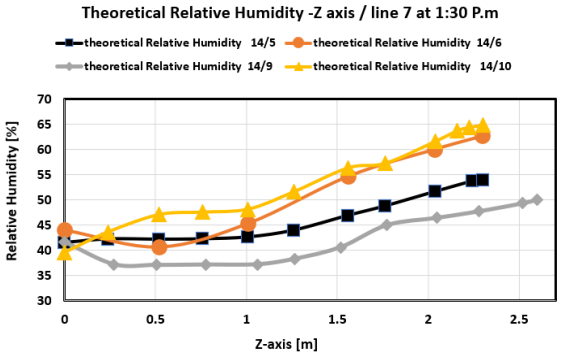

Chart 17. Relative humidity for four months at Y=2 m, X=2 m

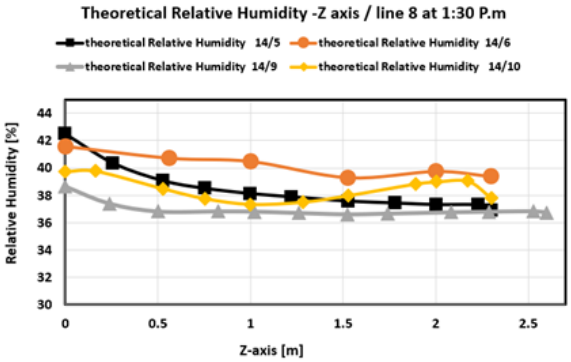

Chart 18. Relative humidity for four months Y=2 m, X=3 m

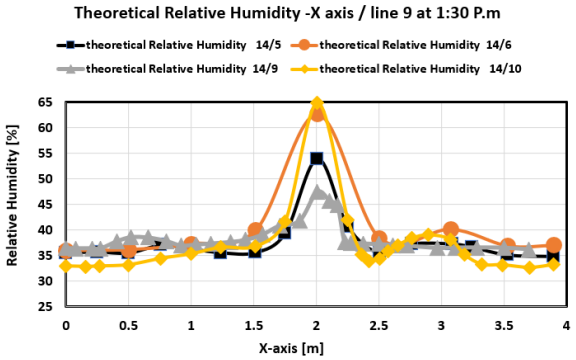

Chart 19. Relative humidity for four months at Z=2.5 m, Y=2 m.

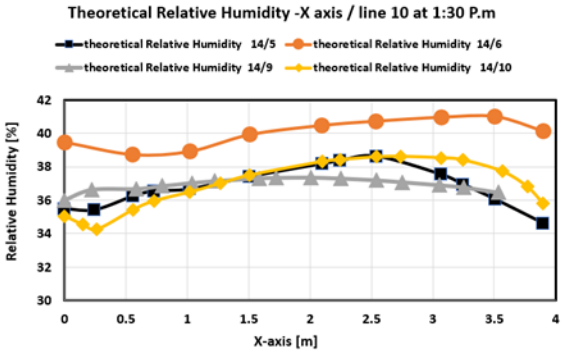

Chart 20. Relative humidity for four months at Z=1.65 m, Y=1.6 m.

In the holy city of Najaf, interior temperatures undergo significant variations during the summer, spanning from May to mid-October. The temperatures gradually rise from May, peak in September, and then improve in October. Environmental shifts play a significant role in these temperature changes. Analyzing Table 10, it is observed that indoor relative humidity increased from 38.6% in May to 41.2% in June, decreased in September, and then rose again in October. The data was generally well-maintained, highlighting the importance of maintaining the circulation of exterior air to prevent moisture accumulation. The relationship between temperature and humidity is dynamic: higher temperatures reduce the air's moisture-holding capacity, thereby decreasing humidity while cooling the air increases humidity. In essence, higher temperatures can accommodate more moisture without a significant increase in humidity. Conversely, lower temperatures can elevate humidity levels. Using both cooling devices simultaneously can improve humidity and cooling conditions.

Evaporative air coolers effectively lower temperatures in dry, hot areas with low humidity. However, their usage in high-humidity conditions might lead to discomfort and dew formation. Combining a desert air cooler

with a standard air conditioner requires careful humidity management to avoid issues like dew and air congestion. Striking the right balance between humidity and temperature is crucial for optimal comfort. The selection and use of these devices should consider individual preferences and environmental factors, aiming to enhance comfort and health in hot, dry conditions.

Table 10. Comparison between the relative humidity of straight lines on the 14th day for four months

Lines	May 14th	June 14th	Sep 14th	Oct 14th
1	37.4	39.7	37.1	37.7
2	38.1	39.7	37.3	38.2
3	36.4	38.6	36.2	36.3
4	40.2	45.6	39.0	41.3
5	37.7	40.4	36.7	38.1
6	37.0	35.8	35.7	34.5
7	46.3	51.2	42.3	53.8
8	38.5	40.2	37.0	38.5
9	37.6	40.9	38.4	37.1
10	36.8	400	36.9	36.9
Ave/TH.[%]	38.6	41.2	37.7	39.2

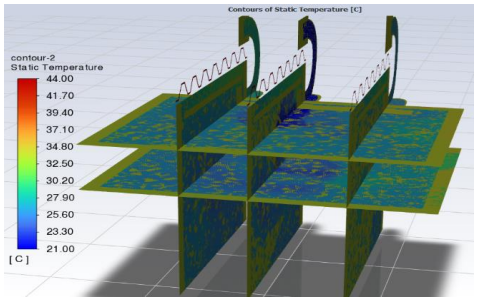

Figure 16. Five planes of temperatures at two inlets and one outlet air

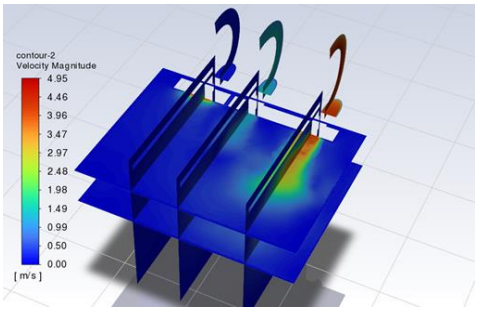

Figure 17. Five planes of velocity contour at two inlets and one outlet air

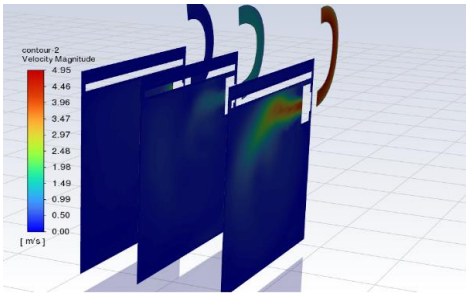

Figure 18. Three planes of velocity

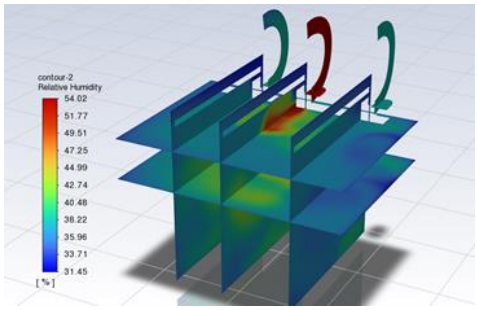

Figure 19. Five planes of relative humidity

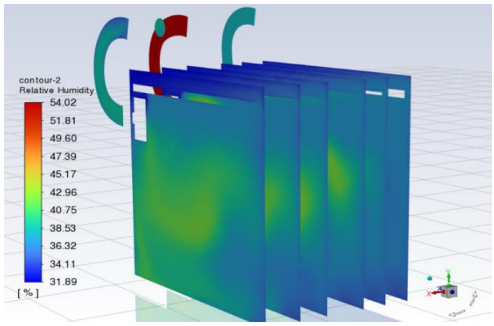

Figure 20. Five planes of relative humidity contour two inlets and one outlet

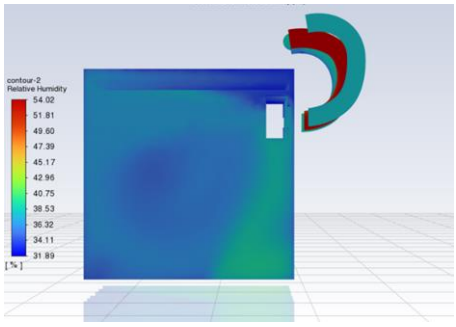

Figure 21. One plane of relative humidity contour in one inlet (no.1)

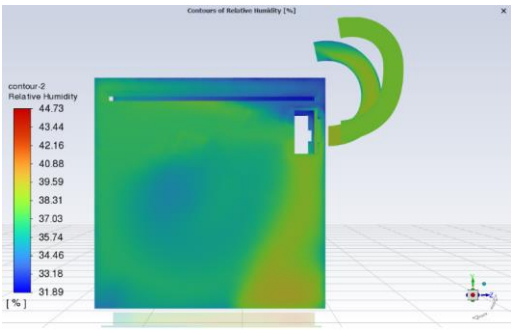

Figure 22. One plane for relative contour in one outlet (no.1)

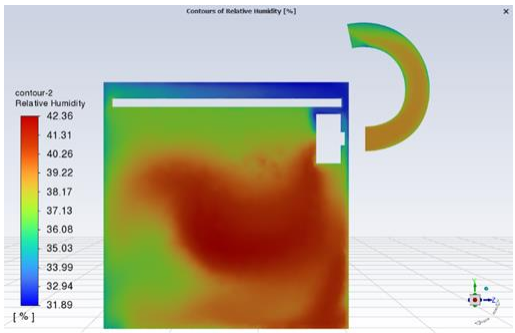

Figure 23. One plane for relative humidity contour in one inlet (no.2)

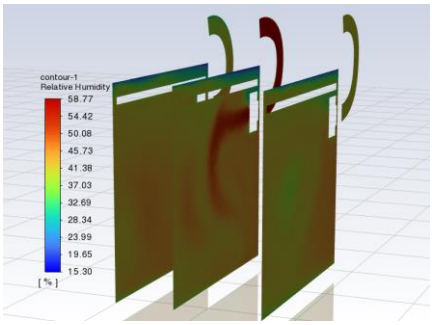

Figure 24. Three planes of relative humidity contour

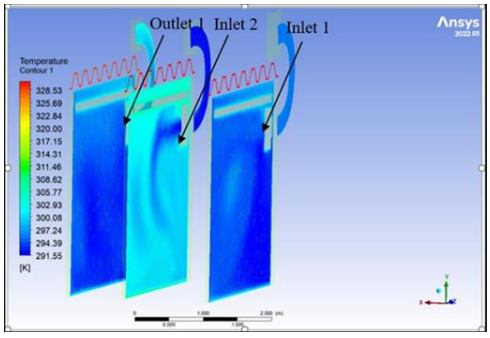

Figure 25. Three planes of temperature contour in two inlets and one outlet air

5.2. Predicted mean votes

The PMV serves as an initial step in assessing room comfort. It relies on equations derived from theoretical principles, delineating comfort levels by differentiating cooling and heating gradients, denoted by negative and positive numbers, respectively. The internal conditions observed on the 14th day of summer testing at 1:30 p.m., as presented in Table 11, depict fluctuations in interior temperature and relative humidity. Despite these variations, the results were deemed acceptable.

Table 11. PMV values and comparison between the months on the same day

Months	Louver vent case	Times (hr)	Temp (°C)	RH%	PS (N/m^2)	PV (N/m^2)	PMV	Case
May	open	1:30 P.M	28	38.6	3.74	1.44	0.40	N
June	closed	1:30 P.M	28.5	41.2	3.85	1.54	0.55	N
Sep	closed	1:30 P.M	27.5	37.7	3.64	1.37	0.26	N
Oct	closed	1:30 P.M	24.5	39.2	3.06	1.20	-0.52	N

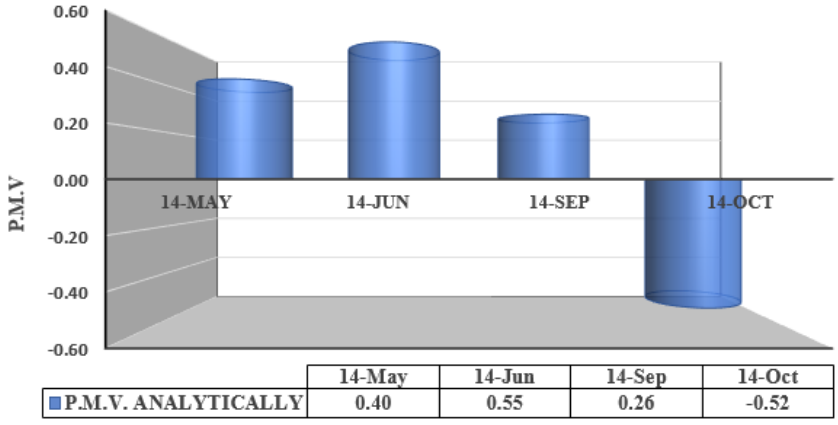

Chart 21. PMV values and comparison between the months on the same day

5.3. Water production efficiency

Water productivity from the return of humid, cool air during summer is particularly notable in managing hot and dry outdoor conditions. Table 12 illustrates that closing the louver air vent can elevate internal humidity, leading to the intake of humid, cool return air. As a result, this process amplifies moisture production, particularly noticeable in June, September, and October in comparison to May. By taking into account these factors and refining water extraction processes, it's plausible to enhance the efficiency of dehumidification systems, especially in coping with hot and dry outdoor conditions.

Table 12. Value of water productivity (analytically) in four months on the same day (14th)

Date	Time	Louver case	A	V a.c	ρ air	M air
May 14th	13:30	open	0.07	1.25	1.2	0.105
June 14th	13:30	closed	0.07	1.5	1.2	0.126
Sep 14th	13:30	closed	0.07	2	1.2	0.168
Oct 14th	13:30	closed	0.07	1.5	1.2	0.126
T out	**RH% out**	**Average temp.**	**Average RH%**	**W1 out**	**W2 room**	**M water room (L/hr)**
37	20	28	38.6	0.00802	0.00928	0.476
40.9	13.5	28.5	41.2	0.00699	0.01019	1.452
37.55	13.5	27.5	37.7	0.00571	0.00877	1.851
32.6	14	24.5	39.2	0.00442	0.00759	1.438

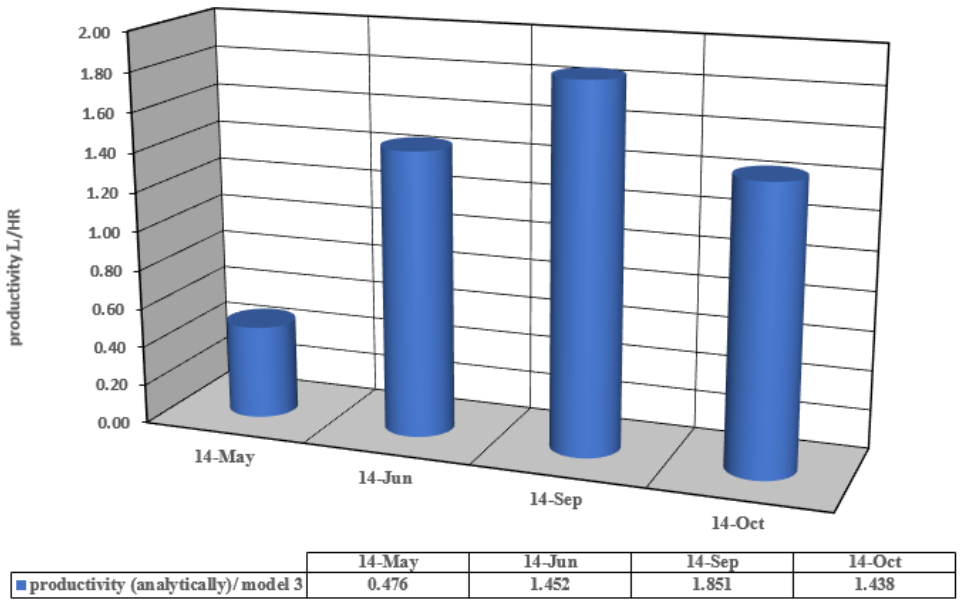

Chart 22. Values of water productivity (analytically) in four months on the same day

6. Conclusion

This study delineated a numerical simulation investigation aimed at enhancing the performance of AC systems by integrating a window-type air conditioner with a DEC-based air conditioning unit. The simulation setup incorporated an integrated window-type air conditioning system with an evaporative air cooler, allowing for various temperature conditions to be generated. The findings highlight that the integration of DEC significantly enhances both the PMV standard and water production when saturated cold air is cycled back to the air conditioner. The combined AC and EC system results in an augmentation of the refrigeration capacity. Moreover, the compressor's electricity demand decreases with every degree of air velocity-related temperature

reduction. Consequently, the DEC-improved system is recommended for usage, especially in extremely humid climates.

Declaration of competing interest

The authors declare that they have no known financial or non-financial competing interests in any material discussed in this paper.

Funding information

No funding was received from any financial organization to conduct this research.

References

[1] B. Niemczuk, A. Nieoczym, J. Caban, and A. Marczuk, "Analysis of chemical and energy properties of energy willow in the industrial burning," *Przemysl Chemiczny*, vol. 97, no. 1, pp. 44–48, 2018, doi: 10.15199/62.2018.1.4.

[2] A. Chlebnikovas *et al.*, "Possibilities and generated emissions of using wood and lignin biofuel for heat production," *Energies (Basel)*, vol. 14, no. 24, Dec. 2021, doi: 10.3390/en14248471.

[3] L. Pérez-Lombard, J. Ortiz, C. Pout, and *-Poutc@bre Co Uk, "A REVIEW ON BUILDINGS ENERGY CONSUMPTION INFORMATION."

[4] P. S. Scalize *et al.*, "Use of condensed water from air conditioning systems," *Open Engineering*, vol. 8, no. 1, pp. 284–292, Feb. 2018, doi: 10.1515/eng-2018-0031.

[5] T. Sonawane, S. Patil, A. Dube, B. D. Chaudhari, T. R. Sonawane, and S. M. Patil, "A Review on Evaporative Cooling Technology," *International Journal of Research in Advent Technology*, vol. 3, no. 2, 2015, [Online]. Available: https://www.researchgate.net/publication/295448903

[6] T. O. Ahmadu, Y. S. Sanusi, and F. Usman, "Experimental evaluation of a modified direct evaporative cooling system combining luffa fiber—charcoal cooling pad and activated carbon dehumidifying pad," *Journal of Engineering and Applied Science*, vol. 69, no. 1, p. 63, 2022, doi: 10.1186/s44147-022-00116-1.

[7] F. W. Yu and K. T. Chan, "Improved condenser design and condenser-fan operation for air-cooled chillers," *Appl Energy*, vol. 83, no. 6, pp. 628–648, 2006, doi: 10.1016/j.apenergy.2005.05.007.

[8] R. Hashim, S. Hammdi, and A. Eidan, "Evaporative Cooling: A Review of its Types and Modeling," *Basrah journal for engineering science*, vol. 22, no. 1, pp. 36–47, Apr. 2022, doi: 10.33971/bjes.22.1.5.

[9] A. Laknizi, M. Mahdaoui, A. Ben Abdellah, K. Anoune, M. Bakhouya, and H. Ezbakhe, "Performance analysis and optimal parameters of a direct evaporative pad cooling system under the climate conditions of Morocco," *Case Studies in Thermal Engineering*, vol. 13, Mar. 2019, doi: 10.1016/j.csite.2018.11.013.

[10] E. Hajidavalloo and H. Eghtedari, "Performance improvement of air-cooled refrigeration system by using evaporatively cooled air condenser," *International Journal of Refrigeration*, vol. 33, no. 5, pp. 982–988, Aug. 2010, doi: 10.1016/j.ijrefrig.2010.02.001.

[11] J. M. Wu, X. Huang, and H. Zhang, "Theoretical analysis on heat and mass transfer in a direct evaporative cooler," *Appl Therm Eng*, vol. 29, no. 5–6, pp. 980–984, Apr. 2009, doi: 10.1016/j.applthermaleng.2008.05.016.

[12] K. R. Aglawe, M. S. Matey, and N. P. Gudadhe, "Experimental Analysis of Window Air Conditioner using Evaporative Cooling." [Online]. Available: www.ijert.org

[13] M. H. Alhamdo, M. A. Theeb, and J. J. Abdulhameed, "Using Evaporative Cooling Methods for Improving Performance of an Air-cooled Condenser," *Universal Journal of Mechanical Engineering*, vol. 3, no. 3, pp. 94–106, May 2015, doi: 10.13189/ujme.2015.030304.

[14] A. K. Dhamneya, S. P. S. Rajput, and A. Singh, "Thermodynamic performance analysis of direct evaporative cooling system for increased heat and mass transfer area," *Ain Shams Engineering Journal*, vol. 9, no. 4, pp. 2951–2960, Dec. 2018, doi: 10.1016/j.asej.2017.09.008.

[15] K. Sellami, M. Feddaoui, N. Labsi, M. Najim, M. Oubella, and Y. K. Benkahla, "Direct evaporative cooling performance of ambient air using a ceramic wet porous layer," *Chemical Engineering Research and Design*, vol. 142, pp. 225–236, Feb. 2019, doi: 10.1016/j.cherd.2018.12.009.

[16] J. R. Camargo, C. D. Ebinuma, and J. L. Silveira, "Experimental performance of a direct evaporative cooler operating during summer in a Brazilian city," *International Journal of Refrigeration*, vol. 28, no. 7, pp. 1124–1132, Nov. 2005, doi: 10.1016/j.ijrefrig.2004.12.011.

[17] M. Q. Shaheen and S. H. Hmmadi, "Combined evaporative air cooler and refrigeration unit for water purification and performance enhancement of air cooling system," *University of Thi-Qar Journal for Engineering Sciences*, May 2019, doi: 10.31663/tqujes.10.1.357(2019).

[18] S. H. Hammadi and O. Kadhim Japer, "Studying the performance of evaporative cooler using pre-cooling water system," 2018. [Online]. Available: http://jeng.utq.edu.iq

[19] E. Hajidavalloo, "Application of evaporative cooling on the condenser of window-air-conditioner," *Appl Therm Eng*, vol. 27, no. 11–12, pp. 1937–1943, Aug. 2007, doi: 10.1016/j.applthermaleng.2006.12.014.

[20] P. Sarntichartsak and S. Thepa, "Modeling and experimental study on the performance of an inverter air conditioner using R-410A with evaporatively cooled condenser," *Appl Therm Eng*, vol. 51, no. 1–2, pp. 597–610, 2013, doi: 10.1016/j.applthermaleng.2012.08.063.

[21] G. N. Tolesa and T. S. Workneh, "CFD modeling of airflow inside unloaded evaporative cooler, Coolbot-air-conditioner and combined operations," in *Acta Horticulturae*, International Society for Horticultural Science (ISHS), Leuven, Belgium, Apr. 2020, pp. 293–302. doi: 10.17660/ActaHortic.2020.1275.40.

[22] F. South, T. Usf, D. Graduate, G. Usf, D. Theses, and H. Begdouri, "Analysis Of The Impact Of The Location Of A Window Type Air-Analysis Of The Impact Of The Location Of A Window Type Air-Conditioner On Thermal Comfort In An Office Room Conditioner On Thermal Comfort In An Office Room Scholar Commons Citation Scholar Commons Citation," 2005. [Online]. Available: https://digitalcommons.usf.edu/etd

This page intentionally left blank.